



HAL
open science

Depth of Martian Magnetization From Localized Power Spectrum Analysis

Shengxia Gong, Mark Wieczorek

► **To cite this version:**

Shengxia Gong, Mark Wieczorek. Depth of Martian Magnetization From Localized Power Spectrum Analysis. *Journal of Geophysical Research. Planets*, 2021, 126 (8), 10.1029/2020JE006690 . hal-03365703

HAL Id: hal-03365703

<https://hal.science/hal-03365703>

Submitted on 8 Aug 2022

HAL is a multi-disciplinary open access archive for the deposit and dissemination of scientific research documents, whether they are published or not. The documents may come from teaching and research institutions in France or abroad, or from public or private research centers.

L'archive ouverte pluridisciplinaire **HAL**, est destinée au dépôt et à la diffusion de documents scientifiques de niveau recherche, publiés ou non, émanant des établissements d'enseignement et de recherche français ou étrangers, des laboratoires publics ou privés.

Copyright

Key Points:

- The depth of magnetization on Mars is investigated using localized power spectrum analyses
- Magnetization is on average 9 km deep north of the dichotomy boundary, but is 32 km deep south of the dichotomy
- The strongest magnetic anomalies are associated with deep magnetization

Supporting Information:

Supporting Information may be found in the online version of this article.

Correspondence to:



S. Gong,
sxgong@shao.ac.cn

Citation:

Gong, S., & Wiczorek, M. (2021). Depth of martian magnetization from localized power spectrum analysis. *Journal of Geophysical Research: Planets*, 126, e2020JE006690. <https://doi.org/10.1029/2020JE006690>

Received 14 APR 2021
Accepted 21 JUL 2021

Depth of Martian Magnetization From Localized Power Spectrum Analysis

Shengxia Gong^{1,2}  and Mark Wiczorek² 

¹CAS Key Laboratory of Planetary Sciences, Shanghai Astronomical Observatory, Chinese Academy of Sciences, Shanghai, China, ²Université Côte d'Azur, Observatoire de la Côte d'Azur, CNRS, Laboratoire Lagrange, Nice, France

Abstract Magnetic field measurements show that Mars possesses strong crustal magnetic anomalies that formed when the planet had an active dynamo. To investigate the origin of this magnetization, we used localized power spectrum analyses to constrain the equivalent depths of thin magnetic layers in the crust. Using a new martian magnetic field model that incorporates data from both the Mars Atmosphere and Volatile Evolution and Mars Global Surveyor missions, we found that the equivalent magnetization depths on Mars vary from the surface to 72 km. In the northern hemisphere the magnetization depths are found to be on average 9 km, whereas in the southern hemisphere the depths are on average 32 km. If these depths are interpreted in terms of a thick magnetic layer, magnetization in the northern lowlands could extend from the surface to about 18 km depth, whereas for the southern highlands the magnetic layer could extend from about 20 km depth to the base of the crust. The strongest magnetic anomalies are, in general, associated with deep source depths. Our results are consistent with the hypothesis where strong primordial magnetic materials of the northern hemisphere were excavated from the Borealis impact basin, leaving only strong deep remanent magnetization in the southern hemisphere.

Plain Language Summary Mars does not have a global magnetic field at present, but portions of the martian crust were strongly magnetized in the past when a dynamo operated. The origin of these crustal magnetic anomalies is uncertain, and knowledge of the depth of the magnetic minerals could help to discriminate among competing hypotheses. We investigate how the magnetization depth varies across the surface. North of the dichotomy boundary, the magnetization lies close to the surface, while in the southern highlands, the magnetization is located on average 32 km below the surface. One interpretation for the origin and distribution of crustal magnetization is that the strongest magnetic anomalies formed early in martian history and that a large impact event that created the dichotomy boundary removed pre-existing deep crustal magnetization in the northern hemisphere.

1. Introduction

Mars today does not possess a planetary-scale magnetic field generated by a core dynamo. However, orbital magnetic field measurements reveal that portions of its crust are strongly magnetized, and the surface intensity of this field is one or two orders of magnitude greater than that of the other terrestrial bodies in our solar system (Acuña et al., 1999). Paleomagnetic analyses also show that the martian meteorite ALH84001 was magnetized in a long-lived field sometime between 3.9 and 4.1 Ga (Weiss et al., 2002). Together, these observations are best accounted for by the existence of a now extinct core-generated dynamo that magnetized crustal rocks when they cooled below their Curie temperature.

One prominent feature of the martian crustal magnetic field is an apparent dichotomy between strong field strengths in the southern highland crust and weak fields in the northern lowlands (see Figure 1). Similar hemispheric dichotomies are also found in topography and crustal thickness (e.g., Smith et al., 1999; Zuber et al., 2000) as shown in the same figure. In addition to this broad hemispheric magnetization signature, some giant impact basins are either weakly magnetized or have been demagnetized, such as Hellas, Argyre, Isidis, and Utopia. The volcanic provinces of Tharsis and Elysium also are associated with weak fields.

The origin of this large-scale distribution of martian magnetic anomalies remains unresolved, and both exogenic and endogenic mechanisms have been proposed. In terms of exogenic processes, it has been proposed that an enormous Borealis impact in the northern hemisphere (Andrews-Hanna et al., 2008; Marinova et al., 2008; Nimmo et al., 2008) might have excavated primordial crust that carried or was capable

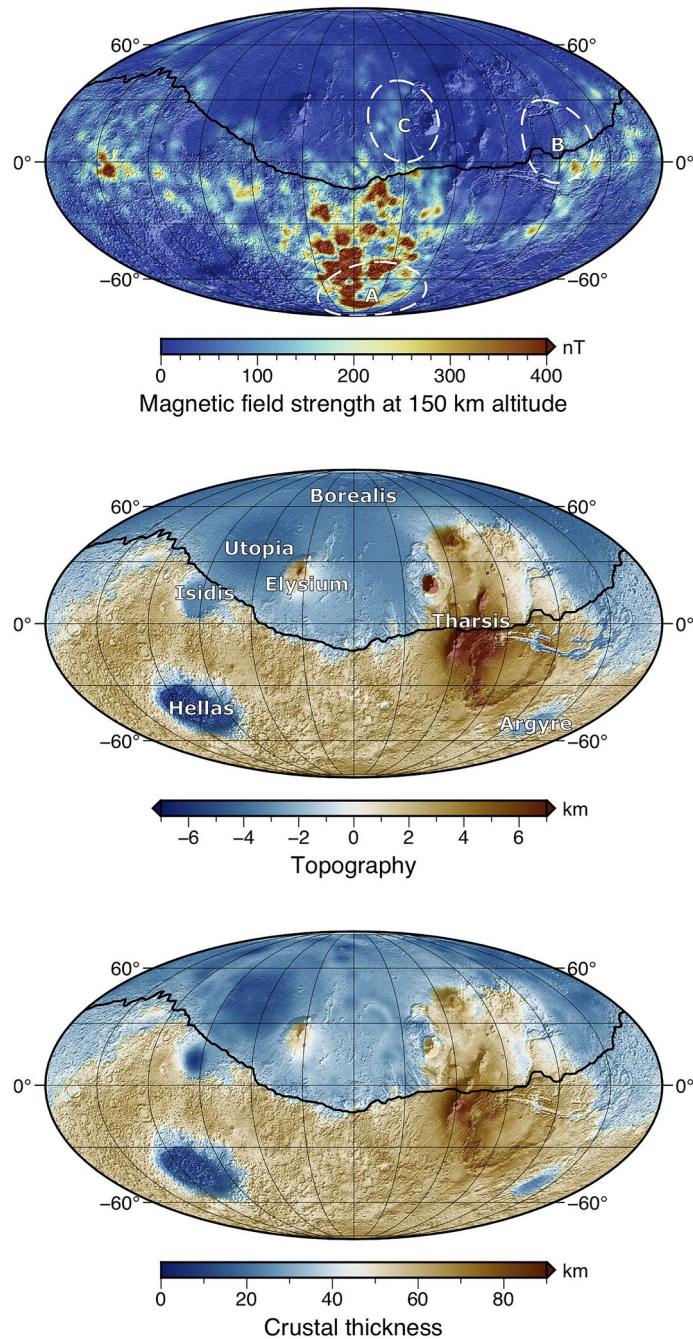


Figure 1. (top) Total magnetic field strength of Mars at 150 km altitude (which corresponds approximately to the periapsis of MAVEN) evaluated using the model of Langlais et al. (2019). The black curve shows the dichotomy boundary of Andrews-Hanna et al. (2008), and the labels A–C correspond to the regions where the example localized power spectra in Figure 2 are calculated. (middle) Topography of Mars (Smith et al., 2001) referenced to the geoid with labeled impact basins and volcanic provinces mentioned in the text. (bottom) Crustal thickness model 2900_5_DWTh2Ref1 of Wicczorek et al. (2020). All maps are presented in Mollweide projections centered over 180°E longitude with grid lines plotted every 30° of latitude and longitude.

of carrying strong magnetization (Mittelholz et al., 2020). For the endogenic models, one proposal is that the difference in magnetic field strength between the two hemispheres could result from the crust being magnetized in a dynamo field that exhibited hemispherical variations in field strength. Models have shown that hemispheric heat flux variations at the core-mantle boundary (e.g., Monteux et al., 2015; Stanley

et al., 2008), or natural convective instabilities (Landeau & Aubert, 2011) could have given rise to dynamo field strengths that are a factor of several stronger in one hemisphere of the planet than the other. However, the observed differences in crustal field strengths between the two hemispheres are much more than a factor of a few. Another set of endogenic models is based on the lithological origin and distribution of these magnetic anomalies. It has been noted that the strongest magnetic anomalies are correlated with the distribution of valley networks (Harrison & Grimm, 2002; Jakosky & Phillips, 2001) and low paleolatitudes after accounting for a potential episode of true polar wander (Hood et al., 2005). In these studies, the magnetic minerals that account for the strong magnetic anomalies were suggested to form by hydrothermal alteration of crustal rocks that was facilitated by higher surface temperatures at low latitudes (see Hood et al., 2005, and reference therein).

In addition to the unexplained hemispheric distribution of crustal magnetism, a related problem is that it is unclear when the magnetic anomalies formed. Given the absence of magnetic signatures within the giant impact basins Hellas, Argyre, and Isidis, which likely formed sometime between 3.8 and 4.1 Ga, it has been proposed that the dynamo either ceased before these basins formed (Acuña et al., 1999; Lillis et al., 2013), or that it initiated after these events (Schubert et al., 2000). Alternatively, the lack of observable magnetic anomalies in these basins could be the result of a thinned crust (Mittelholz et al., 2020). Recent mapping of the crustal magnetic field using Mars Atmosphere and Volatile Evolution (MAVEN) data suggests that a dynamo was operating at both 4.5 and 3.7 Ga based on the presence of magnetic anomalies in the Borealis basin and with a young martian lava flow (Mittelholz et al., 2020), which is consistent with either a long-lived or intermittent dynamo.

One key piece of information that would help discriminate among different formation mechanisms and shed light on the time of magnetization acquisition is the depth of the magnetic sources. Deep magnetic sources might indicate that the magnetization formed either contemporaneously as the primordial crust or later as a result of magmatic intrusions. In contrast, shallow magnetic sources might be associated with impact basin ejecta, surface lava flows, or impact melt sheets. Previous studies on Earth's moon have found that portions of the magnetic sources lie close to the surface (Wieczorek, 2018) and are correlated with surface topography (Gong & Wieczorek, 2020), which is consistent with having an origin as iron-rich impact ejecta. In other regions of the lunar highland crust the magnetization was found to be deep, and likely to have formed with the crust during the initial differentiation of the Moon (Wieczorek, 2018).

The power spectrum of a magnetic field contains information about the geometry and depth of the sources and can be used to investigate the depth of magnetization on Mars. This problem was studied previously for Mars and the Moon by confining the magnetization to either a series of randomly placed magnetized dipoles, prisms, or spherical caps (e.g., Lewis & Simons, 2012; Voorhies, 2008; Wieczorek, 2018). In this study, we make use of a new global magnetic field model that includes data from both the MAVEN and Mars Global Surveyor (MGS) missions, and interpret the power spectrum, localized to regions of interest, in terms of the depth and size of the magnetic sources.

2. Data and Method

We make use of the martian magnetic field model of Langlais et al. (2019), which is expressed in spherical harmonics up to degree and order 134, corresponding to a spatial resolution of ~160 km at the surface. This model is based on a combination of vector magnetic field measurements from the MGS and MAVEN spacecraft, and total field measurements from the MGS electron reflectometer. Given the spherical harmonic expansion coefficients of the model, the Lowes-Mauersberger power spectrum of the total magnetic field strength at radius r is given by (e.g., Lowes, 1966)

$$S_B(l, r) = (l + 1) \left(\frac{a}{r} \right)^{2l+4} \sum_{m=0}^l (g_{lm}^2 + h_{lm}^2), \quad (1)$$

where g_{lm} and h_{lm} are the Schmidt semi-normalized Gauss coefficients of degree l and order m , and a is the reference radius of the magnetic field model which is 3393.5 km. $S_B(l, r)$ provides the contribution to the mean-squared amplitude of the magnetic field strength for the given spherical harmonic degree.

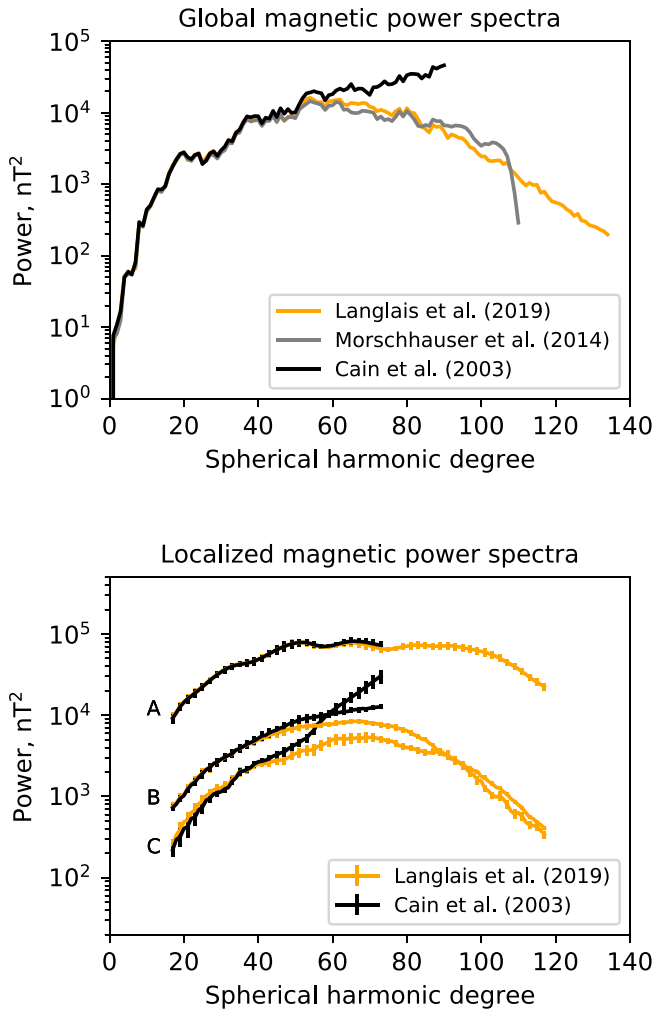


Figure 2. (top) Global magnetic field power spectra of Mars calculated at a radius of 3393.5 km. (bottom) Example localized power spectra with 1- σ uncertainties (calculated at the same radius as the global spectra) for three representative regions (A–C) that were shown in the top panel of Figure 1. The eigenvalue-weighted multitaper localized spectra (shown from degree 17 to $l_{\max} - 17$) were computed using eight localization windows that have an angular radius of 20°, a spectral bandwidth of 17, and that concentrated more than 70% of their power within the region of interest.

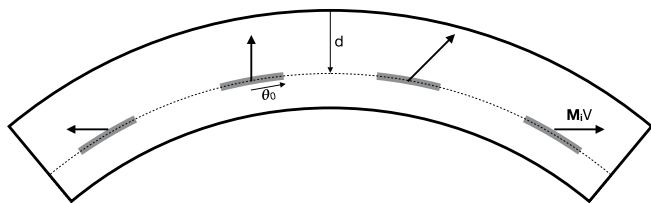


Figure 3. Schematic representation of the stochastic crustal magnetization model. The magnetization is confined to a series of thin spherical caps, each possessing the same volume V , angular radius θ_0 , and depth d . The magnetization vectors \mathbf{M}_i are random, as are the locations of each cap.

The total magnetic field strength of this model is shown in Figure 1, and here we plot its magnetic power spectrum in Figure 2. For comparison, we also plot the power spectra of the model of Cain et al. (2003) that was used in the localized spectral analysis study of Lewis and Simons (2012), as well as the most recent pre-MAVEN model of Morschhauser et al. (2014). As shown in the figure, the power spectrum of the Langlais et al. (2019) model is comparable to the Morschhauser et al. (2014) model up to about degree 80. After this degree, the two slightly diverge until degree 107 when the Morschhauser et al. (2014) model abruptly declines. The spectral behavior of this model, however, is dramatically different from the earlier model of Cain et al. (2003). In particular, beyond degree 55, the power spectrum of the Cain et al. (2003) model continuously increases with respect to the other two models up to the maximum degree. Given that the power spectrum represents a measure of the energy of the magnetic field as a function of the degree, this indicates that the energy is increasing at smaller scales, which is plausibly attributed to undamped noise in their global model. The spectral behavior of the Cain et al. (2003) has not been reproduced in subsequent works, and we thus chose the model of Langlais et al. (2019) to perform the analyses.

We interpret the spectral behavior of the magnetic field by use of a stochastic magnetization model from Wieczorek (2018). In this model, which is similar to the model of Voorhies et al. (2002), the magnetization is confined to a series of individual thin spherical caps, each with the same volume V and depth d below the surface. The magnetization and direction of magnetization are assumed to be random, as shown in Figure 3. This model improves upon the model used by Lewis and Simons (2012) where the magnetization was confined to point dipoles, and is a simplification of the finite-thickness magnetized sill model in Wieczorek (2018). Though Wieczorek (2018) was able to invert for both the depths to the top and bottom of the magnetized region for the Moon, we found that this was not possible for Mars given the comparatively lower spatial resolution of the magnetic field model. Later, in Section 4.1, we will discuss how our model magnetization depths using thin spherical caps relate to those obtained from the more complex model that considers finite thickness magnetized caps. We simply note here that the depths are approximately equal to the midpoint of the magnetized layer when the magnetized layer is thin (less than about 30 km).

By averaging over the magnetization directions and strengths, the theoretical magnetic power spectrum of the model can be shown to be given by

$$\langle S_B(l, r) \rangle = N \langle M^2 \rangle V^2 \left\{ \mu_0^2 \frac{(l+1)(l+2)^2}{12} \left(\frac{h}{r} \right)^2 \left(\frac{r_s}{r} \right)^{2l+2} \times \left[\frac{1}{2} \left(\int_{\cos\theta_0}^1 \bar{P}_{l1}(x) \bar{P}_{l1}(x) dx + \frac{\bar{P}_{l1}(\cos\theta_0) \sin\theta_0 \cos\theta_0}{(l+2)} \right)^2 \right. \right. \quad (2)$$

$$\left. \left. + \left(\int_{\cos\theta_0}^1 \bar{P}_{l0}(x) \bar{P}_{l0}(x) dx - \frac{\bar{P}_{l0}(\cos\theta_0) \sin^2\theta_0}{l+2} \right)^2 \right] \frac{1}{V^2} \right\}.$$

In this equation, $N \langle M^2 \rangle V^2$ is a product that involves the number of caps N and their mean-squared dipole moment $\langle M^2 \rangle V^2$, μ_0 is the magnetic constant ($4\pi \times 10^{-7} \text{ T m A}^{-1}$), V is the volume of a single magnetized cap

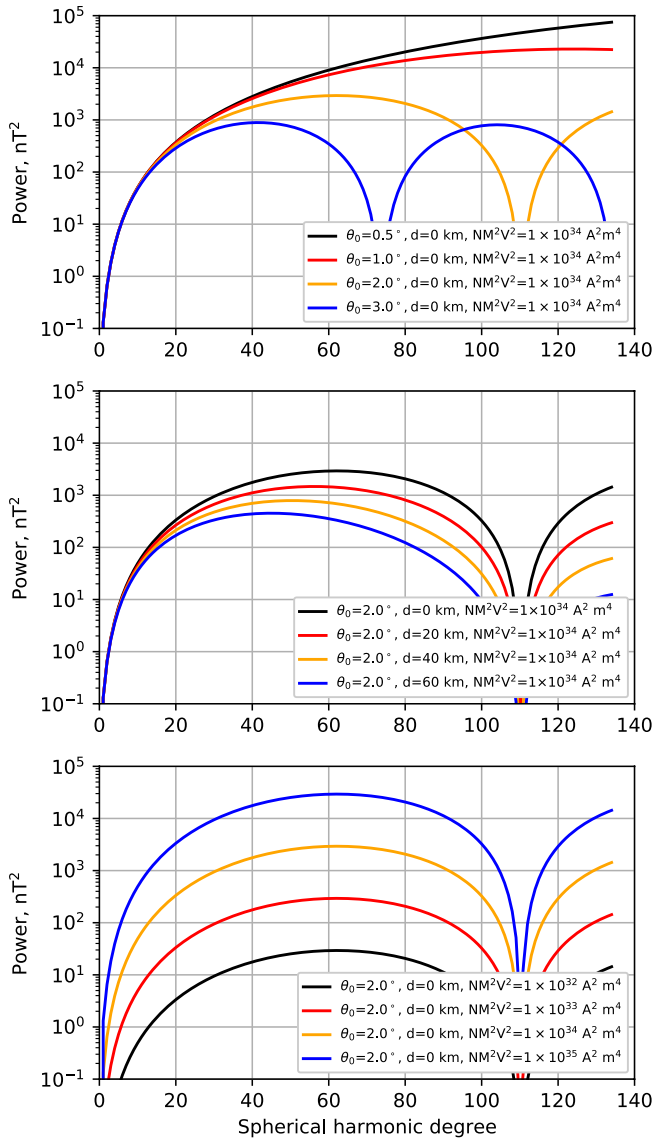


Figure 4. Example theoretical magnetic field power spectra. From top to bottom, the figures show the dependencies of the power spectrum on the angular radius of the magnetized caps, the depth of magnetization, and a parameter related to the total mean-squared magnetic moment of the magnetized caps $N\langle M^2 \rangle V^2$.

of thicknesses h , that is $2\pi r_s^2 h(1 - \cos\theta_0)$, θ_0 is the angular radius of the cap, r_s is the spherical radius where the cap is located in Mars, and \bar{P}_{lm} are the Schmidt semi-normalized associated Legendre functions. The depth of magnetization d is thus the difference between the surface radius of Mars and the radius of magnetization r_s . Example power spectra for various parameters are shown in Figure 4. In general, the amplitude of the spectrum depends primarily on the parameter $N\langle M^2 \rangle V^2$, and the depth of magnetization determines how quickly the spectrum decreases with increasing spherical harmonic degree.

We use a localized power spectrum analysis technique (Wieczorek & Simons, 2005, 2007) to quantify lateral variations in the depth, size, and strength of the magnetic sources on Mars. We follow closely the analysis procedure of Wieczorek (2018), which is briefly summarized as follows. A set of orthogonal windows were first constructed with a given spectral bandwidth l_{win} and angular radius θ . From these spectra, we then formed a multitaper average using the equation

$$S_U^{(\text{mt,obs})}(l, r) = \sum_{k=1}^K a_k S_U^{(k, \text{obs})}(l, r), \quad (3)$$

where $S_U^{(k, \text{obs})}$ is the localized estimate from a single window, and a_k is the weight applied to each window (which sums to unity). In contrast to Wieczorek (2018), who used only windows that concentrated more than 99% of their energy in the region of interest and who set the weights a_k equal to $1/K$, we used the eigenvalue weighting approach of Dahlen and Simons (2008) when calculating the multitaper average, which was found to have slightly better behaved statistical properties. In particular, we used only those windows that concentrated more than 70% of their power within the analysis region, and then set the weights proportional to the localization window's concentration factor. Tests showed that the minimum concentration factor cutoff value used when selecting the windows had little impact on our results. We then converted the localized magnetic potential power spectra into localized power spectra of the magnetic field strength using the equation (see Wieczorek, 2018):

$$S_B^{(\text{mt,obs})}(l, r) = (l+1)(2l+1) \left(\frac{a}{r} \right)^{2l+4} S_U^{(\text{mt,obs})}(l, r) / a^2. \quad (4)$$

Next, for a given set of inversion parameters we computed theoretical, localized power spectra for a range of model parameters. To do this, the global theoretical power spectrum of the magnetic field S_B was computed by Equation 2. The localization procedure modifies that global spectrum, and this was accounted for using the theoretical relation (e.g., Wieczorek & Simons, 2007):

$$\langle S_B^{(\text{mt})}(l, r) \rangle = \sum_{j=0}^{l_{\text{win}}} \left(\sum_{k=1}^K a_k S_h^{(k)}(j) \right) \sum_{i=l-j}^{l+j} S_B(i, r) \left(C_{j0i0}^{l0} \right)^2, \quad (5)$$

where C_{j0i0}^{l0} is a Clebsch-Gordan coefficient, S_h and S_B are the power spectra of the window h and theoretical global magnetic field strength respectively, and a_k is the same weight as used in Equation 3. The localized theoretical power spectrum is similar to a convolution of the global spectrum and the power spectrum of the windows.

Finally, we used a reduced χ^2 function to quantify the goodness of fit between the observations and model. The root-mean-square misfit between the theoretical and observed power spectra was computed from l_{win} to $l_{\text{max}} - l_{\text{win}}$ using the relation

$$\chi^2 = \frac{1}{l_{\max} - 2l_{\text{win}} - 3} \sum_{l=l_{\text{win}}}^{l_{\max}-l_{\text{win}}} \left(\frac{S_B^{(\text{mt,obs})}(l, r) - \langle S_B^{(\text{mt})}(l, r; N\langle M^2 \rangle V^2, \theta_0, r_s) \rangle}{\sigma^{(\text{mt,obs})}(l)} \right)^2, \quad (6)$$

where l_{\max} is the maximum available degree of the magnetic field model, $\langle S_B^{(\text{mt})} \rangle$ is the localized theoretical magnetic power spectrum calculated from Equation 5, and $\sigma^{(\text{mt,obs})}$ is simply the standard error of the K eigenvalue weighted power spectra. Performing a grid search over the inversion parameter space, the best fitting parameters that minimize χ^2 were obtained. After obtaining the best fitting values, a Monte Carlo technique was then employed to quantify the $1\text{-}\sigma$ uncertainties of each parameter (see Gong & Wieczorek, 2020; Wieczorek, 2018). In this step, a global magnetic field power spectrum was first calculated using the best fitting parameters. A global synthetic magnetic field model with random coefficients h_{lm} and g_{lm} was then generated that have the same statistical properties as the theoretical one (i.e., the Lowes-Mauersberger power spectrum of the synthetic model is nearly identical to the theoretical model that is predicted by Equation 2). Next, a localized analysis was performed on the synthetic magnetic field and the best fitting model parameters were determined by minimizing the χ^2 function of Equation 6. The best fitting χ^2 was saved for each simulation, and this procedure was repeated 1,000 times to quantify the probability distribution of χ^2 . From this probability distribution, the 68% confidence level of χ^2 was determined, which was then used to define the $1\text{-}\sigma$ uncertainties of the model parameters.

3. Results

For our analyses, we chose the localization region to be a spherical cap with an angular radius of 20° (diameter of $\sim 2,400$ km) and set the spectral bandwidth to 17, which provides eight localization windows that concentrated more than 70% of their power within the region of interest (three of these have concentration factors greater than 99%). Our localization windows have the same size as those employed in Lewis and Simons (2012), but their bandwidth was lower ($l_{\text{win}} = 8$), in part because of the lower resolution magnetic field model that was available at the time. Our higher bandwidth employed for the localization windows gives rise to a larger number of well localized windows, and better statistical properties of the multitaper localized spectra. Example localized power spectra are shown in the lower panel of Figure 2 for three representative regions that were plotted in Lewis and Simons (2012) using the magnetic field models of Langlais et al. (2019) and of Cain et al. (2003). Though one of the three analyses has similar localized magnetic power spectra using the two different magnetic field models, two regions in the northern hemisphere where the total magnetic field strengths are weak are quite different.

We performed localized spectral analyses and inverted for the model parameters on a quasi equal-area spaced grid that covered the martian surface with a grid spacing of 10° at the equator (~ 600 km). At each location, the observed and theoretical magnetic power spectra were computed at 150 km altitude above the reference radius of the magnetic model, which is the radius where the spherical harmonic model was initially developed in Langlais et al. (2019). Localized power spectra were calculated using the same eight localization windows as above. The misfit between the observed and theoretical localized power spectra was computed from degree 17 to 117, given the maximum degree of 134 and the window bandwidth of 17. The best fitting model parameters were determined as those that minimized the misfit function. We performed Monte Carlo simulations on an equal-area spaced grid with a coarser grid spacing of 30° at the equator, and the obtained 68% confidence levels of χ^2 were found to vary across the surface of Mars from 2.0 to 3.4. For computation convenience, we interpolated the 68% confidence level of χ^2 to each region of interest. The uncertainties of the parameters were then obtained by accepting all models that fit the data within the 68% confidence interval as determined from the Monte Carlo simulations. As was to be expected, some of our analyses could not fit the observed power spectrum within the 68% confidence limits (in particular, 16%, as opposed to 32% that would be expected for Gaussian and stationary errors).

We start by discussing the inversion results for the square root of $N\langle M^2 \rangle V^2$. As shown in Figure 5, the best fitting values of this parameter vary across the surface by almost two orders of magnitude, with those in the southern hemisphere being generally one order of magnitude higher than those in the northern hemisphere. To first order, this parameter mimics that of the total magnetic field strength. This behavior

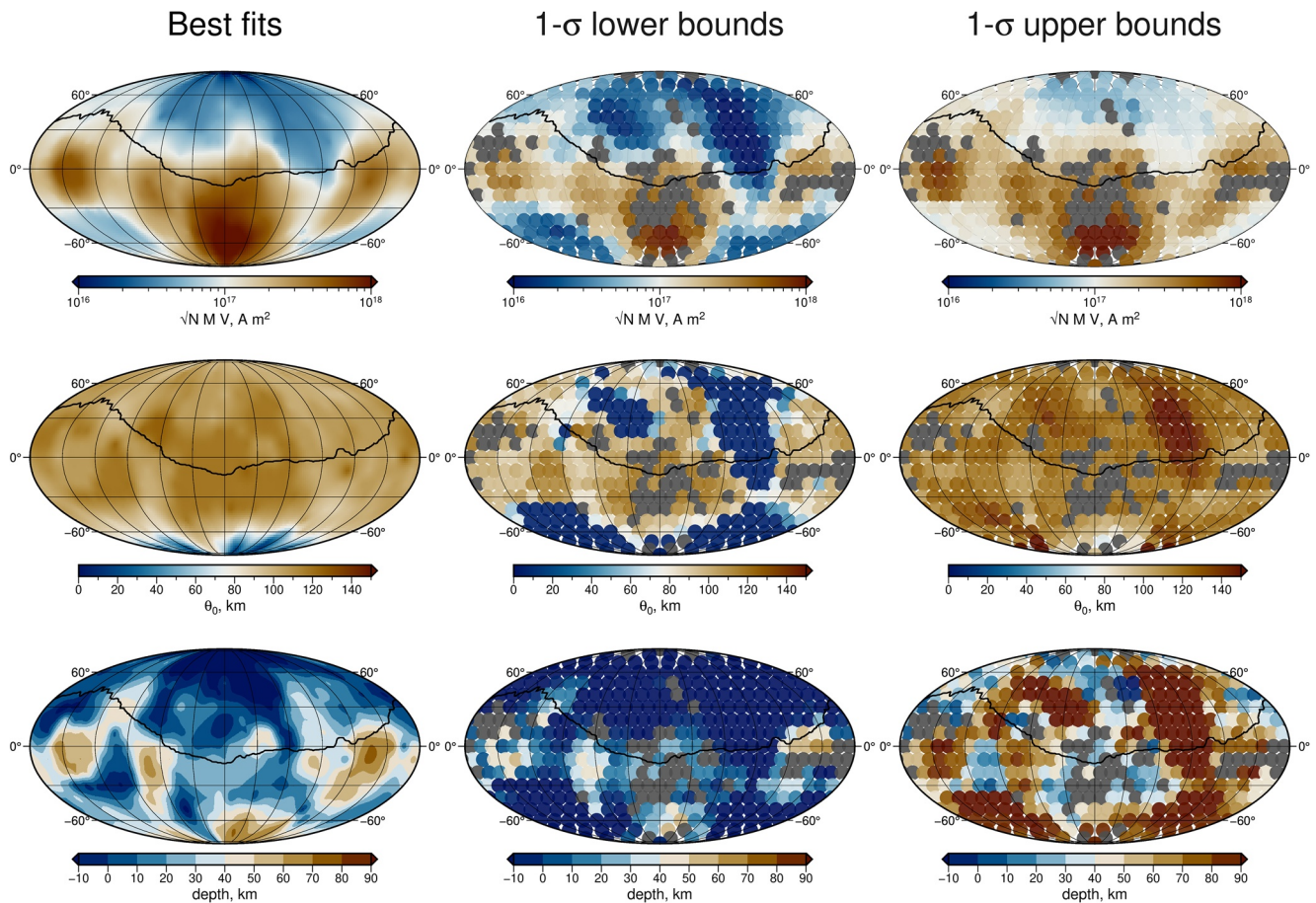


Figure 5. Inversion results. From top to bottom are maps of the square root of $N\langle M^2 \rangle V^2$ that is related to the total dipole moment of magnetization, the radius of the magnetized caps, and the depth of magnetization below the local surface. From left to right are shown the best fitting values interpolated over the entire surface and the $1\text{-}\sigma$ lower and upper bounds for each parameter at the analysis regions. The $1\text{-}\sigma$ bounds are plotted in gray when the best fitting value has a misfit that is greater than its 68% confidence interval as determined from Monte Carlo simulations. For context, the black curve shows the dichotomy boundary of Andrews-Hanna et al. (2008). All maps are presented using the same projection as in Figure 1.

is straightforward and easy to understand: $N\langle M^2 \rangle V^2$ dominates the amplitude of the theoretical magnetic power spectrum, and we would thus expect to have high values of this parameter wherever the magnetic field intensity is high. For the majority of the regions, the uncertainty of this parameter is less than $\pm 50\%$.

The next parameter we discuss is the angular radius of the magnetized caps. For the vast majority of our analyses, the best fitting radii are 90–120 km, and only close to the South Pole do we find smaller values that are a few tens of kilometer. The uncertainties of this parameter are well constrained for most regions, with $1\text{-}\sigma$ limits of $\sim 80\text{--}130$ km. However, a few notable regions that are associated with weak magnetic field strength are found to have larger uncertainties. These regions include the Tharsis province, the Elysium volcanic rise, and the Hellas and Argyre impact basins. These larger uncertainties are plausibly attributed to the relatively lower signal-to-noise ratio of the magnetic field measurements over these regions.

The last parameter to discuss is the depth of magnetization. We referenced this depth to the local average planetary radius within each analysis region, and to test the sensitivity of our models to this parameter, we allowed for magnetization to lie above the surface (with negative depths). As found in Lewis and Simons (2012), we find negative depths of magnetization in some regions, particularly north of the dichotomy boundary. Negative values are unphysical, but we note that within uncertainties, these regions are (with only one single exception) consistent with having the magnetization within the crust. The spatial distribution of this parameter is heterogeneous. Shallow best fitting depths are found in the northern lowlands (ranging from above the surface to 54 km), and within the southern highlands, the depths vary from near

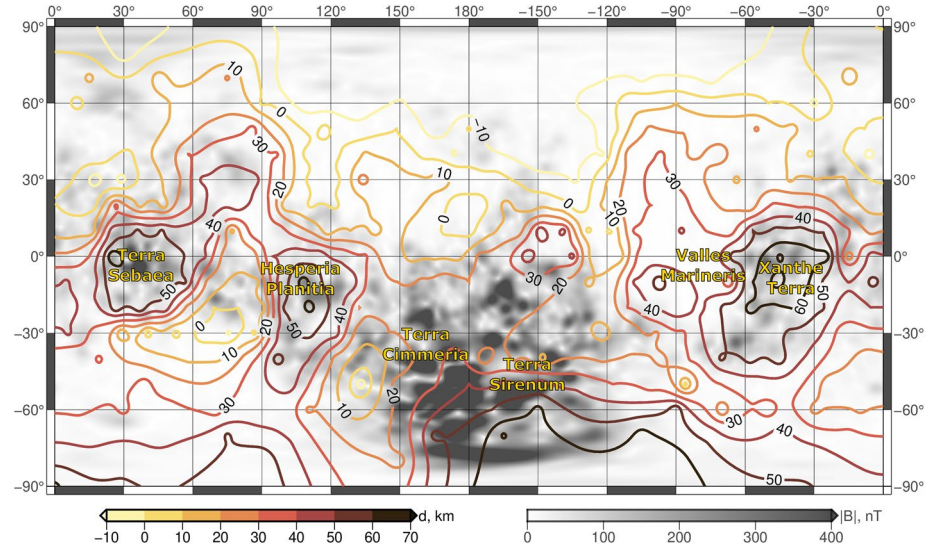


Figure 6. Contour map of the depth of magnetization superposed on a map of the total magnetic field strength from Figure 1. Contours are plotted with a depth interval of 10 km.

the surface to values as high as 72 km. The global average depth of magnetization is 22 km, but the average depths north and south of the dichotomy are 9 and 32 km, respectively.

The four most prominent regions with best fitting depths greater than 40 km, as shown in Figure 6, include a broad region southeast of Terra Cimmeria (34.7°S , 145°E) that extends to the south of Terra Sirenum (39.7°S , 210°E), a region in Xanthe Terra (3°N , 312°E) that is near the eastern end of Valles Marineris (13.9°S , 300.8°E), and two regions in Terra Sabaea (2°N , 42°E) and Hesperia Planum (22.3°S , 110°E). All of these regions are associated with strong surface magnetic field strength. Moderate best fitting depths of magnetization greater than 20 km are also associated with the strong fields north of Terra Cimmeria and Terra Sirenum between about 0 and 30°S .

There is a great difference in the depth of magnetization between the northern lowlands and southern highlands. As shown in Figure 7, the best fitting magnetization depths within the northern lowlands are all less than 60 km with about only 10% being greater than 35 km. Those within the southern highlands are much deeper with more than 50% being greater than 35 km. The $1\text{-}\sigma$ lower bounds of magnetization depths in the northern lowlands are mostly above the surface, while for the southern highlands more than half of the regions have $1\text{-}\sigma$ lower bounds that lie within the crust. The negative magnetization depths are associated generally with weak magnetic field strengths, and could potentially be an artifact of having a relatively lower signal-to-noise ratio for these regions. With a few exceptions, the $1\text{-}\sigma$ upper bounds of the magnetization depth within both hemispheres are smaller than 110 km (which is approximately the maximum value of the thickness of the crust, as discussed in the following section).

We tested the sensitivity of our inversion results to the parameters used in constructing our localization windows. By generating synthetic magnetic models and performing inversions using localization windows with the same angular radius but different bandwidths, we found that the bandwidth of the window needed to be less than 20 to resolve the size of the magnetized caps. This is because this parameter determines the width of the first lobe of the theoretical power spectrum, as shown in Figure 4. By increasing the window's bandwidth, the maximum degree that we can analyze decreases, allowing only an upper bound on size of the magnetized region to be obtained. Conversely, if the resolution of the magnetic field were locally higher, we would be able to resolve smaller sizes of the magnetized regions. This is plausibly the reason for low magnetization cap sizes near the South Pole, as this region is well resolved as a result of low MGS spacecraft periapses over this region (e.g., Plattner & Simons, 2015). Regardless, when considering the uncertainties of our inversions, we do not require the size of the magnetized regions to be smaller near the South Pole than elsewhere. We also tested using localization windows with angular radii of 16° and 24° , but this did not change in any significant manner our best fitting values.

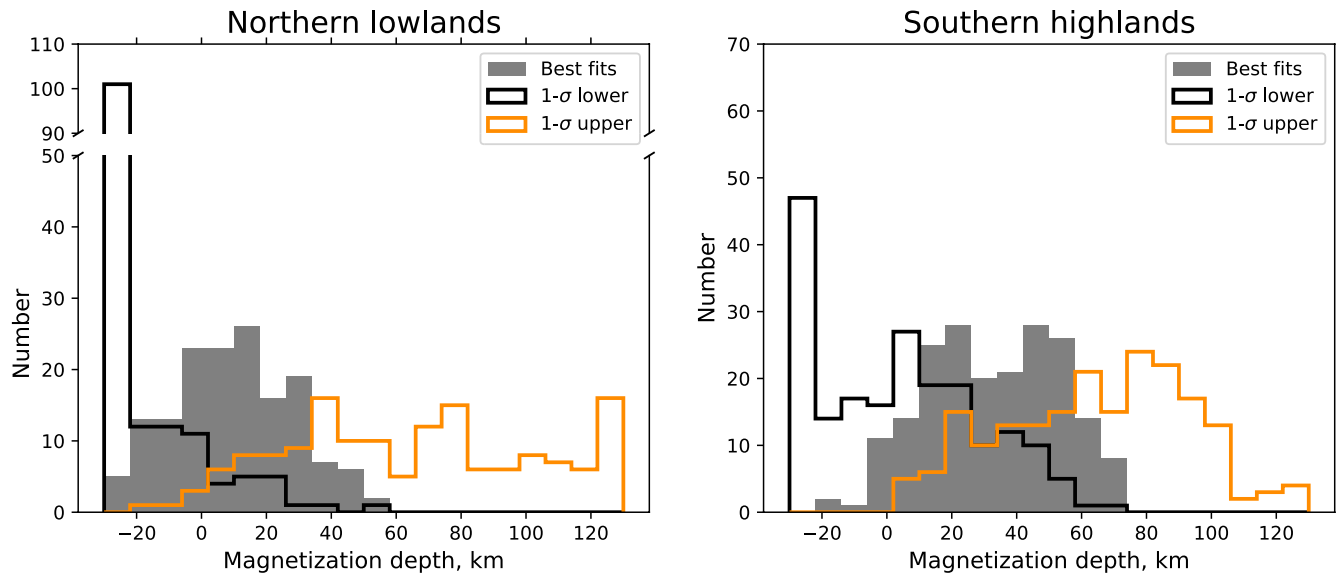


Figure 7. Histograms of the magnetization depths within the northern lowlands (left) and the southern highlands (right). We note that our analyses were performed on an equal-area grid. The best fitting values are shown as gray bars, and the 1- σ lower and upper bounds are outlined in black and orange, respectively. The minimum depth that was investigated was -30 km, which explains the large number of values in this depth bin for the 1- σ lower limit. Note that the y-axis is discontinuous in the left plot.

Given that the highest degree of the magnetic field model could potentially be contaminated by noise, we also performed inversions by truncating the magnetic field model at degrees 90 and 110 (the results are shown in Figures S1 and S2). We found that the results for $N\langle M^2 \rangle V^2$ were unchanged, but that the best fitting cap radius decreased slightly from about 100 km to about 60 km. The best fitting magnetization depths were found to increase somewhat as the degree of truncation decreased. In particular, when only considering the southern highlands, the average depth of magnetization increased from 32 km when using degrees up to 134, to 33 km for degrees less than 110, and to 47 km for degrees less than 90. Nevertheless, as the truncation degree decreased, the uncertainties of the depths increased, reaching nearly a factor of two larger than our baseline analysis when truncating the field at degree 90. The increase in the uncertainty of the depth estimates is simply a result of the smaller number of degrees that can be investigated in these tests.

Finally, we tested how the results would be changed by calculating the magnetic power spectra at the local surface. As shown in Figure S3, the results for the parameter $N\langle M^2 \rangle V^2$ and for the cap's size were unchanged. However, the depth of magnetization was about 10 km shallower than our baseline results, and about 40% of the regions had magnetization above the surface (as opposed to 16% in our baseline analysis). This is likely a result of the amplification of errors when downward continuing the orbital magnetic field measurements to the surface.

4. Discussion

4.1. Depth of Martian Magnetization

The best fitting magnetization depths of our model vary from above the surface to 72 km, with an average value of 22 km. The spatial distribution and the global average of this parameter are consistent with those obtained by Lewis and Simons (2012). In particular, the majority of the deep magnetization was found to be located in the southern highlands and the northern hemisphere is largely associated with shallow magnetization. However, unlike their results, the magnetization depths obtained in our analysis are about 10 km deeper than they obtained for the southern hemisphere. Furthermore, the deepest magnetization depths we found are located near the eastern portion of Valles Marineris (depth of 72_{-16}^{+6} km) and in Terra Cimmeria (depth of 72_{-16}^{+10} km), whereas in their analysis, the deepest magnetization was located in Terra Cimmeria (with depths of 57 km). It is worth noting that we used a better magnetic field model than was available

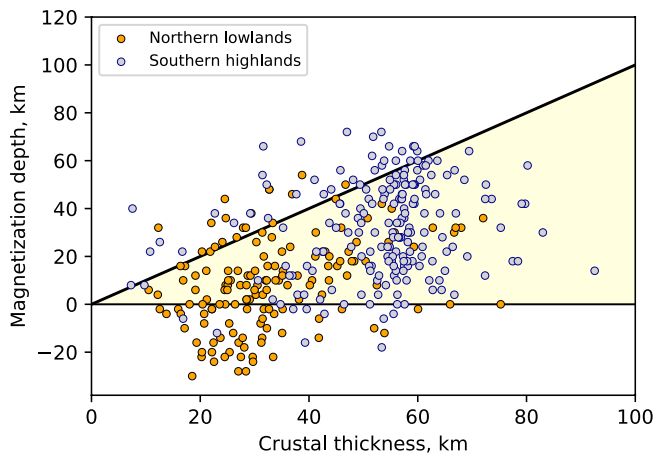


Figure 8. Scatter plot of the magnetization depth with respect to the modeled crustal thickness. The magnetization depths in the northern lowlands are shown in orange and those in the southern highlands are shown in gray. The colored region shows where the magnetization depth is less than the crustal thickness and below the local surface.

assumed thickness at the InSight landing site will change the thickness of both hemispheres by nearly the same amount. Thus, this parameter would not affect our results concerning the relative depths of magnetization in the two hemispheres.

The assumed crustal density affects the lateral variations in crustal thickness. As the density increases and approaches that of the mantle, the amplitude of the crustal thickness variations increases. We have made use of a crustal density of $2,900 \text{ kg m}^{-3}$, which is a reasonable higher-end value based on preliminary analyses of InSight seismic data (Wieczorek et al., 2021). Using a lower crustal density (with the same thickness at the InSight landing site) would give rise to a relatively thinner southern highland crust. This would strengthen our conclusion that the magnetization in the southern highlands extends to the deep crust. If the density of the crust in the northern hemisphere was larger than in the southern hemisphere, this would act only to increase the thickness of the northern hemisphere crust. Thus, a higher density of the northern crust would only strengthen our conclusion that the magnetization is at shallower depths in the northern lowlands than in the southern highlands.

Our analysis used a single magnetization depth to quantify the magnetic power spectrum, similar to previous analyses by Lewis and Simons (2012), Voorhies et al. (2002), and Voorhies (2008). Given that magnetization likely resides in a finite-thickness layer, we investigate how the single depth compares to the depths to the top and bottom of a thick magnetized layer. We first computed the magnetic power spectrum of the finite-thickness magnetized sill model of Wieczorek (2018) for a set of prescribed parameters. Then, using our model of Equation 2 for thin magnetized caps at a single depth, we determined the model parameters that best fit this magnetic power spectrum. In Figure 9, we consider three specific cases where the top of the magnetized layer is at the surface, 40 km depth, and 80 km depth. We then plot our inverted equivalent depth using our single layer model as a function of the depth to the bottom of the magnetized layer for the finite-thickness model. The solid lines plot the depth of the midpoint of the magnetized layer.

As shown in Figure 9, the inverted depth of magnetization using our model with a single depth is nearly identical to the depth of the mid-point when the magnetized layer is thin (less than ~ 30 km). Treating the depth of magnetization as the midpoint of the magnetized layer is a common approximation (e.g., Voorhies et al., 2002). However, as the thickness of the layer increases, our inverted equivalent magnetization depth becomes shallower than the midpoint and is biased toward the surface. Unfortunately, given the spatial resolution of current martian magnetic field models, our analysis cannot constrain the thickness of this layer.

to Lewis and Simons (2012) at the time (see Figure 2), and that we also considered a more realistic magnetization model with extended sources (as opposed to point dipoles).

In Figure 8, we plot the depth of magnetization as a function of crustal thickness. Here we use a crustal thickness model of Wieczorek et al. (2020) which assumes a uniform crustal density of $2,900 \text{ kg m}^{-3}$ and a minimum crustal thickness of 5 km within the Isidis impact basin. This model was previously shown in Figure 1 and has an average crustal thickness of 45 km. We find that the best fitting magnetization depths lie within the crust for 85% of our analyses, and that all magnetization (with only a few exceptions) is consistent with being in the crust when the depth uncertainty is considered (see Figure S4). We emphasize that this crustal thickness model is based on several assumptions that will be tested and improved upon seismic data from NASA's ongoing InSight mission (Banerdt et al., 2020).

As discussed in Wieczorek et al. (2019) and Smrekar et al. (2018), there are three key parameters that affect the global crustal thickness models of Mars: The thickness at the given location (such as the InSight landing site), the crustal density, and whether the crustal density is different in the northern and southern hemispheres. We first note that changing the

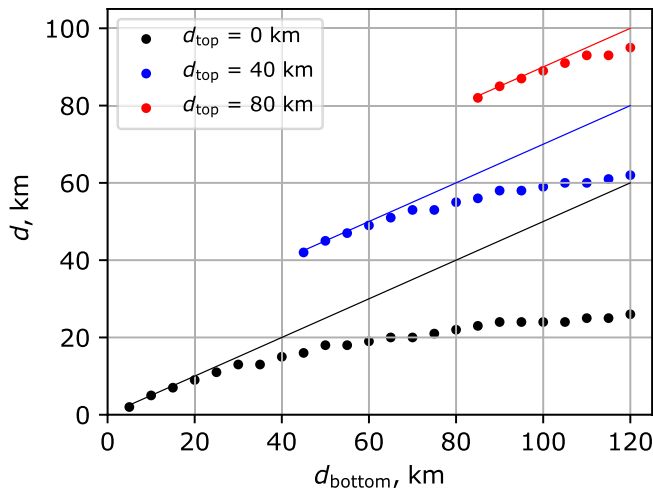


Figure 9. Relationship between the inverted magnetization depth (d) of a thin spherical cap model, and a model that considers magnetization distributed over a finite thickness (from d_{top} to d_{bottom}). Black, blue, and red dots represent the cases where the depth to the top (d_{top}) is set to 0, 40, and 80 km, respectively. Depth to the bottom (d_{bottom}) is varying from close to d_{top} to 120 km. Solid lines show the depths to the mid-point of d_{top} and d_{bottom} .

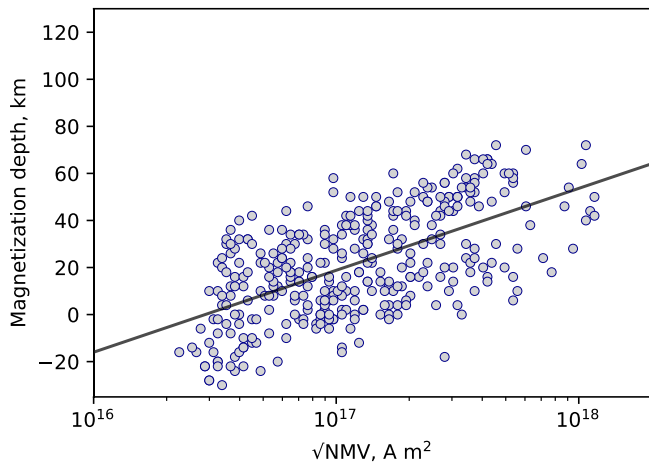


Figure 10. Scatter plot of the magnetization depth as a function of the square root of $N\langle M^2 \rangle V^2$. The black line plots the best fitting linear relationship between these two parameters, where the square of the Pearson correlation coefficient, R^2 , is 0.36.

Based on the above consideration, we can say the following about how magnetization is distributed in the crust. For the northern lowlands, our best fit equivalent depth of magnetization is 9 km. If this is treated as the midpoint of a layer that extends to the surface, the magnetization could extend to a depth of about 18 km. This depth lies within the crust, which is on average 33 km thick in the northern lowlands. For the southern highlands, our best fitting equivalent depth is 32 km. If this is interpreted as a thick layer that extends to the surface, the magnetization would extend to depths much greater than 100 km. These depths are considerably greater than what is predicted by the crustal thickness map used in this study, and it is unlikely that significant magnetization would be found in the upper mantle, especially when considering the elevated temperatures at these depths. If we instead assume that the depth to the bottom of the magnetized layer in the southern hemisphere corresponds to the base of the crust approximately 53 km below the surface, then Figure 9 would imply that the top of the magnetized region would be about 20 km below the surface. In this scenario, the upper portion of the crust would lack a coherent magnetization, perhaps as a result of impact bombardment early in martian evolution.

4.2. Origin of Martian Magnetic Dichotomy

As shown in Figure 1, the magnetic field strengths of the northern lowlands are weak, while those of the southern highlands are strong. Other prominent hemispheric differences have long been noted for Mars, including surface topography and crustal thickness (Neumann et al., 2004; Smith et al., 2001). One explanation for these hemispheric differences is that the northern lowlands formed as a result of a giant Borealis impact (Andrews-Hanna et al., 2008; Marinova et al., 2008; Nimmo et al., 2008). Such an impact would likely remove the entire pre-existing crust of the northern hemisphere and leave a thick impact melt pool in the center of the basin. The magnetic minerals would thus form in a different environment (composition and oxygen fugacity) than did those in the southern highland crust, and they could also have formed at a later date with respect to the southern highlands when the magnetic field strength was potentially lower (e.g., Mittelholz et al., 2020). We note that other small impact basins also have weak magnetizations with respect to their surroundings (e.g., Hellas, Utopia, and Argyre). For these basins, the weak magnetizations and magnetic field strengths are easily explained by the extraordinarily thin crust in their interiors, which would allow for only low quantities of magnetic minerals (assuming they reside in the crust), as discussed by Mittelholz et al. (2020).

In Figure 10, we plot the magnetization depth as a function of the square root of $N\langle M^2 \rangle V^2$, which could be taken as a proxy of the total magnetic field intensity (A similar figure that includes uncertainties is shown in Figure S5). This plot shows that there is a weak correlation, where the deepest magnetization is associated with the strongest magnetic intensities. This suggests that the strongest magnetic anomalies are a result of strongly magnetized sources that are preferentially located deep in the crust. This tendency is contrary to what was found on the Moon, where the strongest magnetic anomalies were found to have shallow source depths (Wieczorek, 2018) and which were proposed to be related to magnetized iron-rich impact ejecta. The hemispherical dichotomy in the magnetization depths and the positive correlation of the magnetization depth and total magnetic field strength could be accounted for by one of the three following scenarios.

The first scenario is that all magnetic anomalies were formed contemporaneously in a primordial crust and were magnetized under a dynamo field that had a hemispherical variation in surface field strength (e.g., Landeau & Aubert, 2011; Monteux et al., 2015; Stanley et al., 2008). Under this scenario, we would expect the magnetization depths of the northern lowlands and southern highlands to show no appreciable difference, which is not what we found in this study. Furthermore, current hemispherical dynamo models can only account for variations of a factor of several between the two hemispheres, whereas the observed strength of magnetization on Mars varies by more than an order of magnitude between the northern and southern hemispheres. Thus, magnetization acquired under a dynamo with hemispherical variations in the surface field strength seems unlikely.

A second scenario is that hydrothermal alteration might have somehow taken part in forming the strongest magnetic anomalies. In this scenario, water might have reacted with ancient atmospheric CO₂ and deposited iron-rich carbonates in the upper crust. Subsequent thermal decomposition of such iron-rich carbonates could give rise to magnetite and generate a strong magnetic source if a dynamo was operating at the time (Scott & Fuller, 2004). The preference of this event occurring within the paleotropics was attributed to the stability of surface water ice at lower latitudes during the early history of Mars (Hood et al., 2005). In this case, one would expect the magnetization depth to be shallow, which is in contrast to what we observe in the southern highlands.

A third scenario, which is our preferred model, is that the giant impact that formed the Borealis basin might have excavated a large portion of crustal material that carried or was capable of carrying strong magnetization within the northern hemisphere (Marinova et al., 2008; Mittelholz et al., 2020; Nimmo et al., 2008). Numerical simulations show that the crust in the northern hemisphere would have been almost entirely removed by such an impact (Marinova et al., 2008; Nimmo et al., 2008), and the thickness of the impact ejecta that would be deposited in the southern highlands was estimated to be 20–25 km on average (Citron & Zhong, 2012). If the ejecta that was deposited in the southern hemisphere was cool, it would not become subsequently magnetized and the observed magnetic signature would come entirely from the pre-existing magnetized crust that was buried 20–25 km beneath the ejecta. Our magnetization depths (when interpreted in terms of a thick layer) are consistent with the lack of appreciable magnetization in the upper 20 km of the southern highland crust. In contrast, if the ejecta was hot, it could have become magnetized as it cooled, if a dynamo field was operating at the time. This would give rise to a thick magnetized layer that extended to the surface, but this scenario is inconsistent with our results that imply the upper 20 km of southern highland crust is not appreciably magnetized. Concerning the shallow magnetic sources found in the northern lowlands, these could be associated with newly formed crust that was thinner within the Borealis impact basin or later thin volcanic flows that erupted at the surface. Mittelholz et al. (2020) suggested that the weak magnetic signatures that are observed in the northern hemisphere are uncorrelated with surface features, which would imply that these lava flows would have been subsequently buried.

5. Conclusion

We used a localized spectral analysis to constrain the strength and equivalent depth of magnetization on Mars. Our results show that (a) the magnetization depths range from above the surface to 72 km beneath the surface with an average value of 22 km, (b) the magnetization depths on Mars show a hemispherical variation with the magnetization in the northern lowlands being close to the surface (on average 9 km) and that in the southern highlands being much deeper (on average 32 km), (3) the spatial distribution of the magnetization depths is loosely correlated with the strength of the crustal magnetization. The coincidence that both the strength and the depth of magnetization behave a hemispherical difference suggests that they might be related to a Borealis impact. During such a giant impact, the pre-existing crust that carried or was capable of carrying strong magnetization could have been excavated from the northern hemisphere, leaving strong magnetic anomalies in the southern highlands that were potentially buried by thick ejecta deposits from this event. Although later magmatic intrusion could be responsible for some of the deep magnetization in the southern highlands, this hypothesis would be difficult to account for the lack of deep and strong magnetic sources in the northern lowlands. Our results also suggest that the martian dynamo was active before or shortly after the Borealis impact (Mittelholz et al., 2020), consistent with either an early dynamo (e.g., Acuña et al., 1999; Lillis et al., 2013) or a long-lived dynamo scenario.

Our analysis, however, was not able to constrain directly the thickness of the magnetized layer. The shallow magnetization of the northern lowlands could be interpreted as a thick magnetized layer that extends from the surface to depths of about 18 km. In contrast, the deeper magnetization depths of the southern highlands could be interpreted as a thick layer that extends from the base of the crust to about 20 km depth. We expect that a higher resolution magnetic field model that incorporates magnetic field observations from future Mars mission will help to constrain the thickness of the magnetized layer.

Data Availability Statement

The magnetic field data used in this study are from Langlais et al. (2019), and the martian topography data are from Wieczorek (2015). The localized spectral analyses used in this study were performed using the software package SHTOOLS (Wieczorek & Meschede, 2018). Most of the figures were created by using the Generic Mapping Tools (Wessel & Smith, 1991). Data plotted in Figure 5 which represent the main results of the study are available in Gong and Wieczorek (2021).

Acknowledgments

The authors thanks Catherine Johnson and two anonymous reviewers for their constructive comments that improved the quality of the study. S. Gong was supported by the B-type Strategic Priority Program of the Chinese Academy of Sciences (Grant No. XDB41000000) and the National Natural Science Foundation of China (Grant No. 11803066). M. Wieczorek was supported by the French Space Agency (CNES).

References

- Acuña, M. H., Connerney, J. E. P., Ness, F. N., Lin, R. P., Mitchell, D., Carlson, C. W., et al. (1999). Global distribution of crustal magnetization discovered by the Mars Global Surveyor MAG/ER experiment. *Science*, 284(5415), 790–793. <https://doi.org/10.1126/science.284.5415.790>
- Andrews-Hanna, J. C., Zuber, M. T., & Banerdt, W. B. (2008). The Borealis basin and the origin of the martian crustal dichotomy. *Nature*, 453(7199), 1212–1215. <https://doi.org/10.1038/nature07011>
- Banerdt, W. B., Smrekar, S. E., Banfield, D., Giardini, D., Golombek, M., Johnson, C. L., et al. (2020). Initial results from the insight mission on mars. *Nature Geoscience*, 13(3), 183–189. <https://doi.org/10.1038/s41561-020-0544-y>
- Cain, J. C., Ferguson, B. B., & Mozzoni, D. (2003). An $n = 90$ internal potential function of the Martian crustal magnetic field. *Journal of Geophysical Research: Planets*, 108(E2), 5008. <https://doi.org/10.1029/2000JE001487>
- Citron, R. I., & Zhong, S. (2012). Constraints on the formation of the martian crustal dichotomy from remnant crustal magnetism. *Physics of the Earth and Planetary Interiors*, 212–213, 55–63. <https://doi.org/10.1016/j.pepi.2012.09.008>
- Dahlen, F. A., & Simons, F. J. (2008). Spectral estimation on a sphere in geophysics and cosmology. *Geophysical Journal International*, 174(3), 774–807. <https://doi.org/10.1111/j.1365-246X.2008.03854.x>
- Gong, S., & Wieczorek, M. A. (2020). Is the lunar magnetic field correlated with gravity or topography? *Journal of Geophysical Research: Planets*, 125(4), e2019JE006274. <https://doi.org/10.1029/2019JE006274>
- Gong, S., & Wieczorek, M. A. (2021). *Depth of martian magnetization from localized power spectrum analysis [Data set]*. Zenodo. <https://doi.org/10.5281/zenodo.4686358>
- Harrison, K. P., & Grimm, R. E. (2002). Controls on Martian hydrothermal systems: Application to valley network and magnetic anomaly formation. *Journal of Geophysical Research*, 107(E5). <https://doi.org/10.1029/2001JE001616>
- Hood, L. L., Young, C. N., Richmond, N. C., & Harrison, K. P. (2005). Modeling of major martian magnetic anomalies: Further evidence for polar reorientations during the Noachian. *Icarus*, 177(1), 144–173. <https://doi.org/10.1016/j.icarus.2005.02.008>
- Jakosky, B. M., & Phillips, R. J. (2001). Mars' volatile and climate history. *Nature*, 412, 237–244. <https://doi.org/10.1038/35084184>
- Landeau, M., & Aubert, J. (2011). Equatorially asymmetric convection inducing a hemispherical magnetic field in rotating spheres and implications for the past martian dynamo. *Physics of the Earth and Planetary Interiors*, 185(3), 61–73. <https://doi.org/10.1016/j.pepi.2011.01.004>
- Langlais, B., Thèbault, E., Houliéz, A., Purucker, M. E., & Lillis, R. J. (2019). A new model of the crustal magnetic field of Mars using MGS and MAVEN. *Journal of Geophysical Research: Planets*, 124(6), 1542–1569. <https://doi.org/10.1029/2018JE005854>
- Lewis, K. W., & Simons, F. J. (2012). Local spectral variability and the origin of the Martian crustal magnetic field. *Geophysical Research Letters*, 39(18), L18201. <https://doi.org/10.1029/2012GL052708>
- Lillis, R. J., Stewart, S. T., & Manga, M. (2013). Demagnetization by basin-forming impacts on early Mars: Contributions from shock, heat, and excavation. *Journal of Geophysical Research: Planets*, 118(5), 1045–1062. <https://doi.org/10.1002/jgre.20085>
- Loves, F. J. (1966). Mean-square values on sphere of spherical harmonic vector fields. *Journal of Geophysical Research*, 71(8), 2179. <https://doi.org/10.1029/JZ071i008p02179>
- Marinova, M. M., Aharonson, O., & Asphaug, E. (2008). Mega-impact formation of the Mars hemispheric dichotomy. *Nature*, 453(7199), 1216–1219. <https://doi.org/10.1038/nature07070>
- Mittelholz, A., Johnson, C. L., Feinberg, J. M., Langlais, B., & Phillips, R. J. (2020). Timing of the martian dynamo: New constraints for a core field 4.5 and 3.7 Ga ago. *Science Advances*, 6(18), eaba0513. <https://doi.org/10.1126/sciadv.aba0513>
- Monteux, J., Amit, H., Choblet, G., Langlais, B., & Tobie, G. (2015). Giant impacts, heterogeneous mantle heating and a past hemispheric dynamo on Mars. *Physics of the Earth and Planetary Interiors*, 240, 114–124. <https://doi.org/10.1016/j.pepi.2014.12.005>
- Morschhauser, A., Lesur, V., & Grott, M. (2014). A spherical harmonic model of the lithospheric magnetic field of Mars. *Journal of Geophysical Research: Planets*, 119, 1162–1188. <https://doi.org/10.1002/2013JE004555>
- Neumann, G. A., Zuber, M. T., Wieczorek, M. A., McGovern, P. J., Lemoine, F. G., & Smith, D. E. (2004). Crustal structure of mars from gravity and topography. *Journal of Geophysical Research*, 109(E8), E08002. <https://doi.org/10.1029/2004JE002262>
- Nimmo, F., Hart, S., Korycansky, D., & Agnor, C. (2008). Implications of an impact origin for the martian hemispheric dichotomy. *Nature*, 453(7199), 1220–1223. <https://doi.org/10.1038/nature07025>
- Plattner, A., & Simons, F. J. (2015). High-resolution local magnetic field models for the martian south pole from mars global surveyor data. *Journal of Geophysical Research: Planets*, 120(9), 1543–1566. <https://doi.org/10.1002/2015JE004869>
- Schubert, G., Russell, C., & Moore, W. (2000). Timing of the martian dynamo. *Nature*, 408(6813), 666–667. <https://doi.org/10.1038/35047163>

- Scott, E. R., & Fuller, M. (2004). A possible source for the martian crustal magnetic field. *Earth and Planetary Science Letters*, 220(1), 83–90. [https://doi.org/10.1016/S0012-821X\(04\)00032-9](https://doi.org/10.1016/S0012-821X(04)00032-9)
- Smith, D. E., Zuber, M. T., Frey, H. V., Garvin, J. B., Head, J. W., Muhleman, D. O., et al. (2001). Mars Orbiter Laser Altimeter: Experiment summary after the first year of global mapping of Mars. *Journal of Geophysical Research*, 106(E10), 23689–23722. <https://doi.org/10.1029/2000JE001364>
- Smith, D. E., Zuber, M. T., Solomon, S. C., Phillips, R. J., Head, J. W., Garvin, J. B., et al. (1999). The global topography of Mars and implications for surface evolution. *Science*, 284, 1495–1503. <https://doi.org/10.1126/science.284.5419.1495>
- Smrekar, S. E., Lognonné, P., Spohn, T., Banerdt, W. B., Breuer, D., Christensen, U., et al. (2018). Pre-mission insights on the interior of mars. *Space Science Reviews*, 215(1), 3. <https://doi.org/10.1007/s11214-018-0563-9>
- Stanley, S., Elkins-Tanton, L., Zuber, M. T., & Parmentier, E. M. (2008). Mars' paleomagnetic field as the result of a single-hemisphere dynamo. *Science*, 321(5897), 1822–1825. <https://doi.org/10.1126/science.1161119>
- Voorhies, C. V. (2008). Thickness of the magnetic crust of Mars. *Journal of Geophysical Research*, 113(E4), E04004. <https://doi.org/10.1029/2007JE002928>
- Voorhies, C. V., Sabaka, T. J., & Purucker, M. (2002). On magnetic spectra of Earth and Mars. *Journal of Geophysical Research*, 107(E6), 5034. <https://doi.org/10.1029/2001JE001534>
- Weiss, B. P., Vali, H., Baudenbacher, F. J., Kirschvink, J. L., Stewart, S. T., & Shuster, D. L. (2002). Records of an ancient Martian magnetic field in ALH84001. *Earth and Planetary Science Letters*, 201(3), 449–463. [https://doi.org/10.1016/S0012-821X\(02\)00728-8](https://doi.org/10.1016/S0012-821X(02)00728-8)
- Wessel, P., & Smith, W. H. F. (1991). Free software helps map and display data. *Eos, Transactions American Geophysical Union*, 72(41), 441–446. <https://doi.org/10.1029/90EO00319>
- Wieczorek, M. A. (2015). Gravity and topography of the terrestrial planets. In G. Schubert (Ed.), *Treatise on geophysics* (2nd ed., pp. 153–193). Elsevier. <https://doi.org/10.1016/B978-0-444-53802-4.00169-X>
- Wieczorek, M. A. (2018). Strength, depth, and geometry of magnetic sources in the crust of the Moon from localized power spectrum analysis. *Journal of Geophysical Research: Planets*, 123, 291–316. <https://doi.org/10.1002/2017JE005418>
- Wieczorek, M. A., Beuthe, M., Rivoldini, A., & Van Hoolst, T. (2019). Hydrostatic interfaces in bodies with nonhydrostatic lithospheres. *Journal of Geophysical Research: Planets*, 124(5), 1410–1432. <https://doi.org/10.1029/2018JE005909>
- Wieczorek, M. A., Knapmeyer-Endrun, B., Panning, M. P., Plesa, A.-C., McLennan, S. M., Nimmo, F., et al. (2021). Global character of the martian crust as revealed by InSight seismic data. *Proceedings of the Lunar and Planetary Science Conference*, 52, 1412.
- Wieczorek, M. A., & Meschede, M. (2018). SHTools: Tools for working with spherical harmonics. *Geochemistry, Geophysics, Geosystems*, 19, 2574–2592. <https://doi.org/10.1029/2018GC007529>
- Wieczorek, M. A., Plesa, A.-C., Knapmeyer-Endrun, B., McLennan, S. M., Nimmo, F., Michaut, C., et al. (2020). Global crustal thickness modeling of Mars using InSight seismic constraints. *Proceedings of the Lunar and Planetary Science Conference*, 51, 1393.
- Wieczorek, M. A., & Simons, F. J. (2005). Localized spectral analysis on the sphere. *Geophysical Journal International*, 162(3), 655–675. <https://doi.org/10.1111/j.1365-246X.2005.02687.x>
- Wieczorek, M. A., & Simons, F. J. (2007). Minimum-variance multitaper spectral estimation on the sphere. *Journal of Fourier Analysis and Applications*, 13, 665–692. <https://doi.org/10.1007/s00041-006-6904-1>
- Zuber, M. T., Solomon, S. C., Phillips, R. J., Smith, D. E., Tyler, G. L., Aharonson, O., et al. (2000). Internal structure and early thermal evolution of mars from mars global surveyor topography and gravity. *Science*, 287(5459), 1788–1793. <https://doi.org/10.1126/science.287.5459.1788>